Characterization of a Compton camera based on the TOFPET2 ASIC

R. Viegas [a,*], J. Roser [a], L. Barrientos [a], M. Borja-Lloret [a], J.V. Casaña [a], J. García López [b,c], M.C. Jiménez-Ramos [b,d], F. Hueso-González [a], A. Ros [a], G. Llosá [a]

[a] *Instituto de Física Corpuscular (IFIC), CSIC-UV, Valencia, Spain*
[b] *Centro Nacional de Aceleradores (Universidad de Sevilla, CSIC and Junta de Andalucía), E-41092 Sevilla, Spain*
[c] *Departamento de Física Atómica, Molecular y Nuclear, Universidad de Sevilla, Sevilla, Spain*
[d] *Departamento de Física Aplicada II, Universidad de Sevilla, 41012 Sevilla, Spain*

ARTICLE INFO

ABSTRACT

The use of Compton cameras for medical imaging and its interest as a hadron therapy treatment monitoring has increased in the last decade with the development of silicon photomultipliers. MACACO$_p$ is a Compton camera prototype designed and assembled at the IRIS group of IFIC-Valencia. This Compton camera is based on monolithic Lanthanum (III) Bromide crystals and silicon photomultipliers, and employs the novel TOFPET2 ASIC as readout electronics. This system emerged as an alternative to MACACO II prototype, with the aim of improving its limited time resolution. To test the performance of the ASIC in a Compton camera setup, the prototype was characterized, both in laboratory and in-beam. A time resolution of 1.5 ns was obtained after time corrections, which improves greatly the performance of the MACACO II. Moreover, the results obtained at high photon energies demonstrate the ability of the system to obtain 1 mm displacements of the reconstructed spots. The results reinforce the potential of the system as a monitoring device for hadron therapy.

1. Introduction

Hadron therapy is a cancer treatment modality based on accelerated charged particles capable of high precision dose delivery to a specific tumour volume, which decreases the dose in surrounding healthy tissue when compared to conventional radiotherapy. Despite this high accuracy, there are uncertainties encountered when such a beam is delivered to the target volume. To avoid the risks associated with these uncertainties, safety margins need to be applied, which can be as much as 3% of the proton range (Paganetti, 2012). To reduce these safety margins, different approaches for in-vivo beam range verification have been proposed. For instance through the detection of secondary particles produced during the irradiation, such as positrons and prompt gammas-rays (Krimmer et al., 2018; Yamaya et al., 2011; Meißner et al., 2019; Verburg and Seco, 2014; Hueso-González and Bortfeld, 2020). Prompt gamma-rays are emitted during the decay of the excited nuclei within picoseconds after the irradiation process and are more abundant than positrons, being a perfect candidate for accurate proton range verification (Verburg et al., 2013). Said secondary radiation can be measured with the use of Compton cameras (CCs), which were first proposed for medical imaging in Todd et al. (1974). The CC uses the registration of successive interactions of the incident photons in position sensitive detectors. From these interactions it is possible to exploit the respective Compton scattering kinematics, allowing for the reconstruction of the origin of incident gamma-rays via the determination of the Compton scattering angle. This imaging system has several advantages over collimated gamma cameras since it presents higher sensitivity and enables the possibility of simultaneously imaging gammas of different energies in a wide energy range (Llosá, 2019). The applicability of CCs for in-vivo range verification has been addressed by several groups (Parajuli et al., 2019; Hueso-Gonzalez et al., 2017; Golnik et al., 2016; Ortega et al., 2015; Liprandi et al., 2017).

The IRIS group of IFIC-Valencia recently developed and fully characterized the second version of a three-layer CC based on monolithic Lanthanum (III) Bromide (LaBr$_3$) crystals coupled to silicon photomultiplier (SiPM) arrays, MACACO II (Medical Applications CompAct COmpton camera). This system uses the VATA64HDR16 ASIC from IDEAS (Meier et al., 2010) as front-end electronics, having obtained an energy resolution (ER) of 5.6% full width at half maximum (FWHM) at 511 keV. Tests with point-like sources (Barrientos et al., 2021) and in-beam (Ros et al., 2020; Muñoz et al., 2021) were carried out with success. An important limitation of this system is its time resolution of 24 ns FWHM (Barrio et al., 2015), mainly due to time-walk.

A timing resolution close to 1 ns FWHM is desired for a CC to be able to correctly reject neutron background (O'Neill et al., 1992; Biegun et al., 2012) and to obtain a more accurate gamma-ray emission

---

* Corresponding author.
E-mail address: Rita.Viegas@ific.uv.es (R. Viegas).

profile (Livingstone et al., 2021), and thus it is a relevant parameter for in-vivo proton therapy monitoring. Moreover, by improving the system's time resolution one can reduce the coincidence time window, thus decreasing the number of random coincidences. Consequently, there will be an improvement of the signal-to-noise ratio, reducing statistical noise and therefore enhancing the image quality. In order to improve the time resolution and to extend the dynamic range, alternative readout electronics have been considered. ASICs with high performance integrated circuits and time-to-digital converters (TDCs) can be employed to achieve time resolution in the order of the ps, without compromising spatial and energy resolution. In the last years several high performance ASICs for medical imaging have become commercially available, such as the Petiroc2A (Ahmad et al., 2020), and the TRIROC (Ahmad et al., 2021) from Weeroc, the HRFlexToT (Sanchez et al., 2022) from ICCUB and the TOFPET2 (Bugalho et al., 2018) from PETsys Electronics, among others.

Most available electronic components for medical imaging detectors were designed for low-count-rate scenarios, leading to event loss and therefore poor intrinsic detection efficiency at high-count-rate environments, such as hadron therapy rooms (Polf et al., 2022). For instance the novel TOFPET2 ASIC was initially designed and optimized for reading Positron Emission Tomography (PET) detector modules, with crystal arrays. However, due to its high readout speed (average 600 kHz/channel), dark counts rejection up to 2 MHz, high time resolution (30 ps binning) and broad dynamic range (up to 1500 pC), it was chosen as readout electronics for the alternative two-layer CC (MACACO$_p$). The work presented aims at assessing the improvements offered by the ASIC TOFPET2 in a scintillator-based Compton camera for hadron therapy treatment monitoring, in particular the timing resolution and dynamic range. MACACO$_p$ was characterized in the laboratory and tested in-beam at the *Centro Nacional de Aceleradores* (CNA, Seville) at high photon energies. The measurements at CNA allowed testing the prototype in a more realistic scenario, and to assess the possibility of obtaining images with photons at the relevant energies for hadron therapy, 4.44 MeV.

The obtained experimental results in the laboratory and at CNA, as well as Monte Carlo simulations, are presented in this work. In Section 2, the experimental setup and measurements performed, both in laboratory and in-beam, are described; in Section 3, the results obtained are shown and compared with the performed simulations. Finally, the results obtained are discussed in Section 4 and the corresponding conclusions are drawn.

2. Materials and methods

2.1. Materials

The CC prototype is composed of two identical detector modules. Each one consists of a $25.8 \times 25.8 \times 5$ mm^3 LaBr$_3$ monolithic scintillation crystal, manufactured by Epic-Crystal, coupled to a Ketek SiPM array (PA3325-WB-0808). Each array has 64 (8×8) elements of 3×3 mm^2 with a micro-pixel pitch size of 25 μm, and a photon detection efficiency of approximately 40% at the wavelength of maximum emission of the LaBr$_3$ (380 nm). Due to their hygroscopicity, the crystals are surrounded by reflective material and encased in an aluminium housing with a quartz window. The photodetectors are enclosed in an opaque plastic holder to prevent ambient light from reaching them.

MACACO$_p$ employs the TOFPET2 ASIC and readout board as readout electronics. This ASIC reads and processes the photosensor signals, providing time and energy digitization of signals from 64 channels. Each channel contains charge integration analog-to-digital converters (ADCs) and TDCs with 30 ps binning, allowing to read out each one individually (Bugalho et al., 2019). The ASIC has a maximum event rate of 600 kHz per channel, low power consumption (<10 mW/channel), low noise and dynamic range up to 1500 pC.

TOFPET2 presents two analog circuit schemes, one for timing and another one for energy, that make use of three discriminators, two on the timing branch (D_T1, and D_T2) and one on the energy branch (D_E) with adjustable thresholds (vth_t1, vth_t2, and vth_e). The first discriminator, D_T1, is set to a low voltage threshold and provides the hit time stamp. The second threshold, D_T2, validates the timing trigger and allows for dark count rejection. In the separate energy branch, the D_E threshold is set to suppress low amplitude signals. For a hit to be validated and digitized, when using the nominal trigger mode, all three thresholds need to be overcome. The threshold values need to be carefully chosen in order to obtain an optimal energy and time resolution, without making the system sensitive to noise or SiPM dark counts.

The system has two acquisition modes, *"qdc"* and *"tot"*. In the former, the output energy measurement is obtained by linear charge integration. In *"tot"* mode the energy measurement is obtained from the time-over-threshold (ToT), using the D_E and D_T1 discriminators time stamps. In the present work, the system was operated in *"qdc"* mode, measuring both the hit time stamp and the signal integrated charge for each channel. Further information about this acquisition system can be found in Bugalho et al. (2019) and Francesco et al. (2016).

Custom printed circuit boards (PCBs) (Fig. 1(b)) were used as an interface between the front-end-modules containing the ASICs and the SiPM arrays.

2.2. Laboratory measurements

Both the SiPMs and ASICs exhibit a temperature-dependent response, therefore the laboratory measurements were performed at a controlled ambient temperature of 20.0 °C ± 0.2 °C by placing the system inside a Dycometal CCK climatic chamber.

2.2.1. Detector characterization

The detector modules were characterized by taking data with a ^{22}Na point-like radioactive source, and the configuration and operating parameters that yield optimal performance were determined. This includes adjusting the applied bias voltage to the SiPM array, determining the values for the thresholds of the acquisition discriminators and the integrator gain. Raw data are acquired after performing an ASIC calibration employing PETsys routines and are then converted into single-raw-hit information and further processed using analysis routines developed by our group. An event is considered as a group of hits that are less than 10 ns apart from the preceding in the sequence. The energy deposited per event is obtained by summing up the 64 ADC measured values. Due to SiPM saturation and ASIC non-linearity (Ferramacho and Tavernier, 2019) a quadratic polynomial was fit to convert the acquired charge values in to keV.

The acquired data were processed in two modes: singles and coincidence. In *singles mode*, the energy deposited in each detector is analysed independently, whereas in *coincidence mode*, events with signals in both planes within a pre-determined coincidence time window (CTW) are considered.

2.2.2. System characterization

The system was mounted in CC mode, as depicted in Fig. 1(a), where the first detector module was placed 60 mm away from the second one (centre-to-centre) and a radioactive source was centred with the first detector at a 60 mm distance. The CTW was set to 10 ns. Coincidence data were acquired with a ^{22}Na point-like source with an activity of 223 kBq at the time of measurement, distributed on an active area with a nominal diameter of 0.5 mm. In order to obtain the Coincidence Time Resolution (CTR), the time difference of the signals produced by the two detectors in time coincidence was histogrammed and fitted with a Gaussian function. The CTR calculation was performed by applying an energy window from 450 keV to 600 keV on the coincidence summed energy spectra, with the detectors in CC mode.
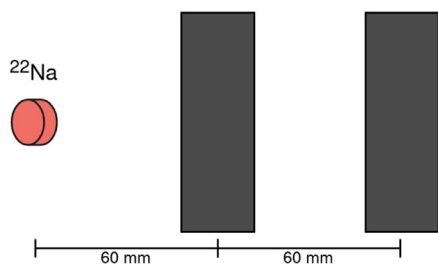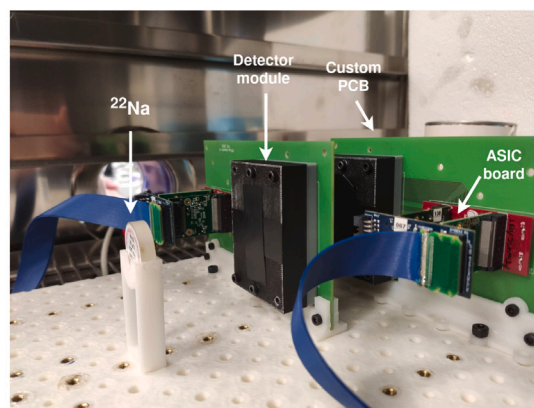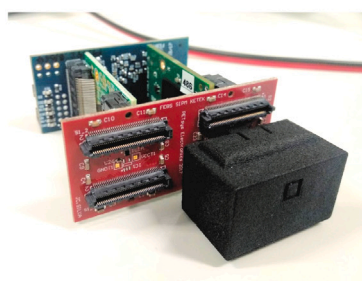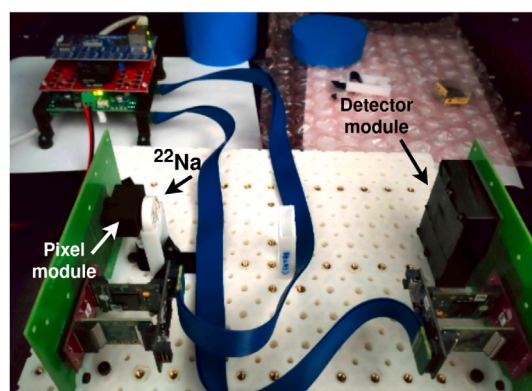
Fig. 1. (a) Compton Camera mode scheme. (b) System setup placed inside the climatic chamber.

Fig. 2. (a) Pixel module composed by a PM3325-WB-D0 (Ketek) SiPM with a 3×3 mm^2 active area coupled to a $3 \times 3 \times 5$ mm^3 LYSO crystal wrapped with teflon. (b) Setup for time-skew corrections. The ^{22}Na radioactive source was centred and placed as close as possible to the pixel module, and the detector module was placed 220 mm away from it.

Time correction. To compensate for the uncertainties in the recorded timestamps, induced by time-skew and time-walk errors, time corrections need to be applied. Time-skew error is a timing error induced by the different paths of the signals among the 64 ASIC channels. The time-walk is the dependency of the timing determination of a signal with its charge amplitude.

First, the time skew was corrected. In order to do so, a reference detector (*pixel module*) composed by a PM3325-WB-D0 (Ketek) SiPM with a 3×3 mm^2 active area coupled to a $3 \times 3 \times 5$ mm^3 LYSO crystal wrapped with teflon, provided by PETsys electronics for reference and system performance verification, was used (Fig. 2(a)). A point-like ^{22}Na radioactive source was attached and centred with the *pixel module*, which was placed 220 mm away from one of the *detector modules* described in Section 2.1 (Fig. 2(b)). In this way, the *detector module* was uniformly irradiated, and therefore the mean values of the timing distributions of all the time stamp differences between each channel of the *detector module* and the *pixel module* should be nearly constant, independently of the collected energy (Lamprou et al., 2020). The gaussian centroids of the time differences from each channel of the *detector module* and the *pixel module* were determined and stored in a look-up table and were later used as an offset calibration for the recorded timestamps in each channel. This procedure was performed for both *detector modules*.

The time-walk corrections were carried out, after applying the time-skew corrections, with the same setup described above (Fig. 2). A 2D plot was generated, for both *detector modules*, of the time difference between the *pixel* and *detector modules* as a function of the collected

energy. For each energy bin a time difference projection was obtained, and the relationship between the mean time (peak centroid) (t_m) and the energy bin centre (E) was identified. The resulting profile can be described empirically with a power series model:

$$t_m = a \times E^b + c \tag{1}$$

where a, b and c are free parameters (Poulson et al., 2020). After determining the fitting parameters the time was corrected for each energy, for both *detector modules*.

Time estimation. Regarding the timing performance, an advantage of the TOFPET2 ASIC is the fact that we can measure the timing of each hit per channel. Rather than only recording a single timestamp per event, we can get a more accurate estimation of the interaction time by using multiple time stamps. Different methods presented in van Dam et al. (2013) were investigated in order to estimate the interaction time, based on the timestamp of the most energetic hit and the average time stamp. The average of the six earliest timestamps recorded per event was finally selected.

2.3. In-beam experiments

In-beam tests were carried out at CNA (Seville). The cyclotron employed is a Cyclone 18/9 from IBA (Ion Beam Applications, Louvain-La-Neuve, Belgium), that accelerates protons and deuterons up to 18 and 19 MeV, respectively (Baratto-Roldán et al., 2018). For the measurements, three currents were set: low (250 pA–410 pA), medium (2.5 nA) and high (3.9 nA). The laboratory ambient temperature was
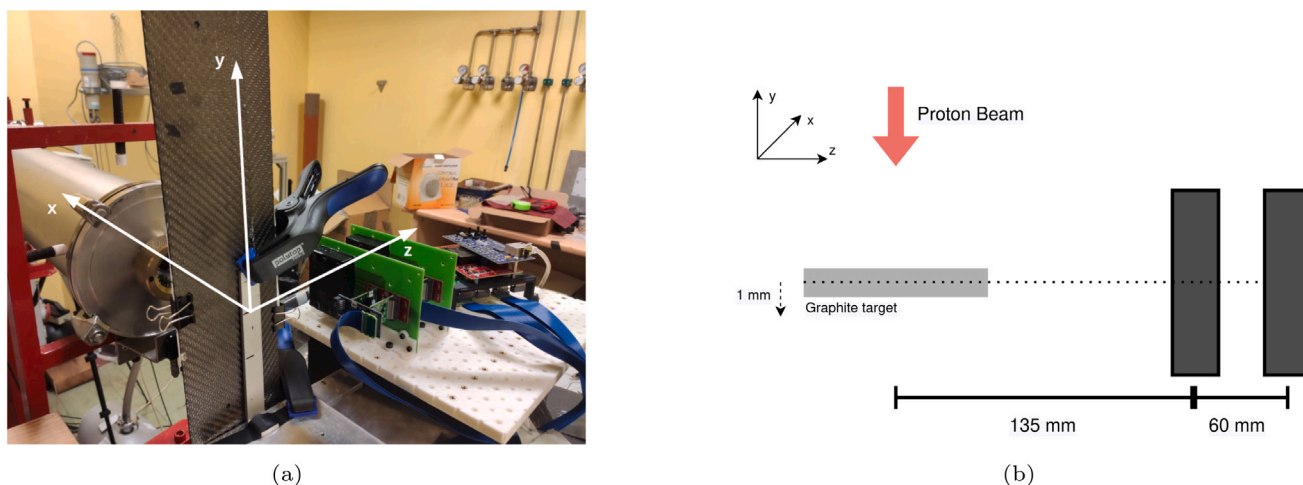
Fig. 3. (a) Setup of the MACACO$_p$ prototype at the CNA beam-line. (b) Diagram of the graphite target and Compton camera setup. The distance between the target and the first plane was set to 135 mm and the distance between the first and second plane was set to 60 mm. The graphite target was moved in steps of 1 mm with a linear motorized stage, along the *x*-direction.

constant throughout the measurements (17 °C). The 18 MeV proton beam available at the experimental line of CNA goes through a 100 μm thick aluminium window and an air gap before reaching a graphite target with an energy of 17.2 MeV. When the beam interacts with the target 4.44 MeV gamma-rays are produced from the inelastic $^{12}C(p,p')^{12}C^*$ reaction (Ros et al., 2020). The graphite target consists of a plate of 3.6 mm thickness and dimensions 8×40 cm^2 placed at 110 mm from the beam exit. The proton beam spot had an area of 8×5 mm^2, measured with a radiochromic film.

A reference detector, consisting of a $51.2 \times 51.2 \times 10$ mm^3 LaBr$_3$ monolithic crystal coupled to a photomultiplier tube (PMT) (Model R6237, Hamamatsu) was set on the opposite side of the CC, 130 mm away from the target, in all performed measurements. Hence, a reference energy spectrum was obtained.

The CC was placed perpendicularly to the beam line. In all measurements, the distance between the target and the first plane centre was set to 135 mm and the distance between the first and second planes (centre to centre) was 60 mm. (Fig. 3(a)). Different measurements were acquired by placing the graphite target at different positions in 1 mm steps along the *x* direction with a linear motorized stage with micrometric precision (± 80 μm), as shown in Fig. 3(b).

2.4. Image reconstruction

The reconstructed images shown in this work were obtained by employing a list-mode maximum likelihood expectation maximization (LM-MLEM) algorithm. The system and sensitivity matrices employed for the reconstruction were calculated with a spectral analytical model for two-plane CCs (Muñoz et al., 2020), in which the emitted photon energy is an unknown parameter as it will be the case in the real scenario.

The data were reconstructed employing a field of view (FoV) of $48 \times 23 \times 13$ spatial voxels of $0.5 \times 1 \times 3$ mm^3 and 10 energy bins linearly distributed in the range 0.2–8.0 MeV. To exclude low energy photons that are not correlated with the deposited dose, a low energy threshold of 200 keV was applied to the data measured in both planes and a threshold of 800 keV was applied to the combined deposited energy. For a smoother visualization, a spatial median filter was employed after the final iteration to all images. All the shown reconstructed images correspond to iteration 50 of the image reconstruction algorithm.

2.5. Detection efficiency

The intrinsic detection efficiency (ε_{int}) of the system was calculated as the fraction of events entering the surface of the first detector module that produce detected coincidence events. MACACO$_p$ detection efficiency was both calculated in the laboratory, with a point-like source, and at CNA, with a proton beam. Both scenarios were also simulated. The ε_{int} can be determined through:

$$\varepsilon_{int} = \frac{N \text{ coincidences}}{A \times t \times \frac{a}{4\pi r^2}} \tag{2}$$

considering *A* the activity of the point-like source (or number of prompt gamma-rays emitted per unit of time), *t* as the acquisition time, *a* the area of the detector and *r* the distance between the source and the first plane of the CC.

For the detection efficiency at high photon energies the fraction of prompt-gammas (PG) yield per photon had to be determined, through the use of GATE (version 8.2) simulations employing the *QGSP_BIC_HP_EMZ* physics list.

2.6. Simulations

The prototype was simulated with GATE version 8.2 (Jan et al., 2011), a Monte Carlo simulation toolkit based on Geant4 version 10.05 (Agostinelli et al., 2003). To reproduce the 4.44 MeV gamma-rays interaction in the detector, a gamma source with such energy was simulated. This way the gamma production in the graphite target was mimicked. The electromagnetic physics list (*emstandard_opt3*) was employed. The detectors were modelled as LaBr$_3$ scintillator crystals, and the SiPMs and plastic holders were also included in the simulations. Moreover, the detector modules were placed at the same distances as in the experimental measurements and the ER of the two detector modules was set to the values obtained experimentally.

3. Results

3.1. Detector characterization

The best detector performance was reached when setting the integrator gain to its maximum value (3.65) and the voltage thresholds, vth_t1, vth_t2, vth_e, to 25, 150, and 100 mV, respectively. All other configuration settings were left to default. The SiPM operating voltage was determined through a bias sweep, in which the best performance was obtained at 29.2 V (24.7 V of breakdown voltage plus 4.5 V of
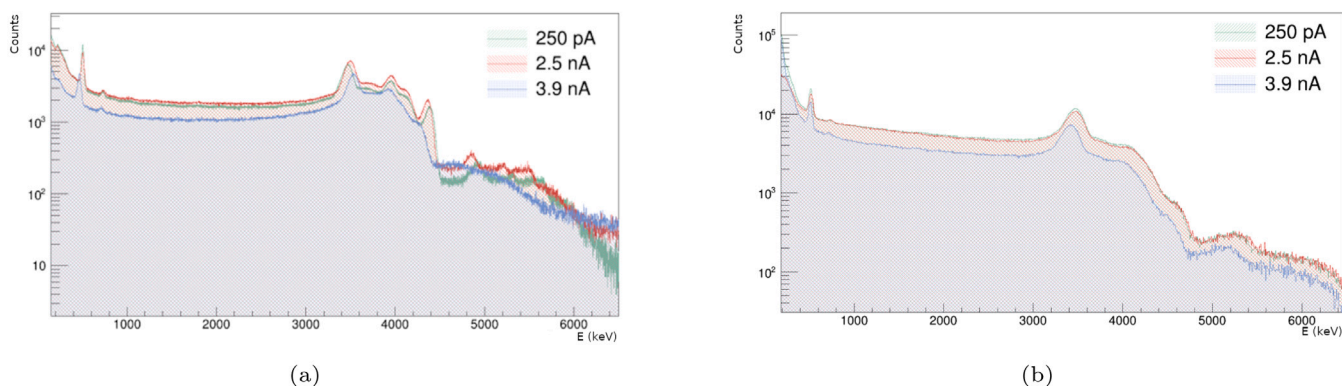
Fig. 4. Energy spectra measured with the PMT reference detector (a) and in singles mode with the first plane of MACACO$_p$ (b), for three different beam currents (250 pA, 2.5 nA and 3.9 nA). The acquisition time was 10 min in all cases.

overvoltage). The ER was calculated by fitting a gaussian function with linear background to the 511 keV peak. ERs of 6.6% and 6.4% at 511 keV were obtained for the first and second plane detectors, respectively, in singles mode.

3.2. Coincidence studies

The results reported in this subsection were obtained with the system working in coincidence mode, as explained in Section 2.2.2.

Without applying any time correction, a CTR, in CC mode, of 3.13 ns FWHM was obtained. After applying the time corrections and estimations explained in Section 2.2.2, an optimal CTR of 1.50 ns FWHM was obtained by averaging the six earliest timestamps recorded per event.

Most CTR values found in the literature were measured in PET mode. For this reason, a measurement of the CTR placing the detector modules in PET mode, facing each other and separated by 12 cm, with a ^{22}Na radioactive source located in the centre, equidistant of the two detector modules, was carried out. A CTR of 820 ps was obtained by applying an energy window between 450 keV and 600 keV to each detector, as explained in Ros et al. (2021). Since the two detector modules are equal, one can calculate the detector time resolution (DTR) as $\sqrt{\frac{\text{CTR}^2}{2}}$, obtaining a value of 580 ps.

3.3. In-beam results

3.3.1. Data in singles mode

Fig. 4(a) shows the energy spectra measured with the PMT reference detector, placed 130 mm away from the target, for the three beam current intensities: low (250 pA), medium (2.5 nA) and high (3.9 nA) beam current. For both the low and medium current measurements, the characteristic energy peaks for the 4.44 MeV photons can be seen with an ER of 2.4%. However, for the high current, only the general expected pattern for the energy spectrum is visible.

With MACACO$_p$, measurements were taken with the target at a distance of 135 mm from the centre of the first plane. In the spectra obtained with the PMT reference detector (Fig. 4(a)) the 4.44 MeV photoabsorption peak can be clearly observed as well as the associated double escape peak at 3.42 MeV caused by the 4.44 MeV gamma-rays undergoing pair production in the detector with the subsequent escape of the annihilation photons (Ros et al., 2020). However, in the spectra obtained with MACACO$_p$'s first detector module (Fig. 4(b)), only the double escape peak can be clearly distinguished, due to the small size of the detector, which reduces the probability of complete absorption of the 4.44 MeV gamma-ray.

3.3.2. Data in coincidence mode

In-beam measurements with MACACO$_p$ in time coincidence were performed, as detailed in Section 2.2.1. Fig. 5 shows the comparison of the measured spectra in coincidence for the three previously mentioned beam currents. The spectra of the energy deposited in the first and second detector modules for different current intensities are shown in Fig. 5(a) and 5(b), respectively. In both cases, the 511 keV peak can be identified, which occurs when the primary gamma-ray undergoes pair production and the coincidence is completed by a secondary annihilation photon. Moreover, the double escape peak of the 4.44 MeV PG, 3.42 MeV, can be distinguished. The sum spectra (Fig. 5(c)) reproduce the shape of those measured in singles mode (Fig. 4(b)). The 4.44 MeV double escape peak, 3.42 MeV, can be seen, but the single escape peak 3.93 MeV and the absorption peak 4.44 MeV are not clearly distinguished.

Fig. 6 shows the comparison between the spectrum obtained in coincidences mode with the low current beam and the one obtained with simulated data. A higher number of coincidences, at lower energies, can be observed in the experimental data, due to background radiation. However, at higher energies both data sets depict the same features.

3.3.3. Reconstructed images

The graphite target was moved in steps of 1 mm in the opposite direction of the beam line, as illustrated in Fig. 3(b). For the low current beam, measurements were performed at 4 different target positions, separated by 1 mm (0, 1, 2 and 3 mm), while the medium and high current measurements were performed with the target at 2 positions, separated by 2 mm (0 and 2 mm). While for the low current beam the acquisition time was 30 min, for the medium and high current beams, it was only of 10 min, in order to get approximately the same statistics in all cases.

For all measured beam currents, the spot was recovered in the spectral extent of the reconstructed 4D image that corresponds to 4.44 MeV, as expected. Therefore, to estimate the separation between target positions, the three-dimensional spatial slice at the aforementioned energy was considered. For each target position, at each beam current, the position of the maximum of the reconstructed photon emission distribution and the positions at R80 (depth at 80%) and R50 (depth at 50%) after the maximum were calculated. The results obtained for each image are listed in Table 1. The source of error considered was the voxel size in the x-dimension with error propagation. Figs. 7, 8 and 9 show the x-profiles (Figs. 7(b), 8(b), 9(b)) and reconstructed images (Figs. 7(a), 8(b), 9(a)) for the low, medium and high current beam, respectively. The x-profiles are obtained by drawing a longitudinal profile along the beam direction (x-direction) at y = 0 mm, since the detector's height was aligned with the centre of the spot irradiated with the target. Moreover, as an example, for the medium current beam, the yE-projection for the initial target position and the energy profiles are depicted (Figs. 8(c) and 8(d)).
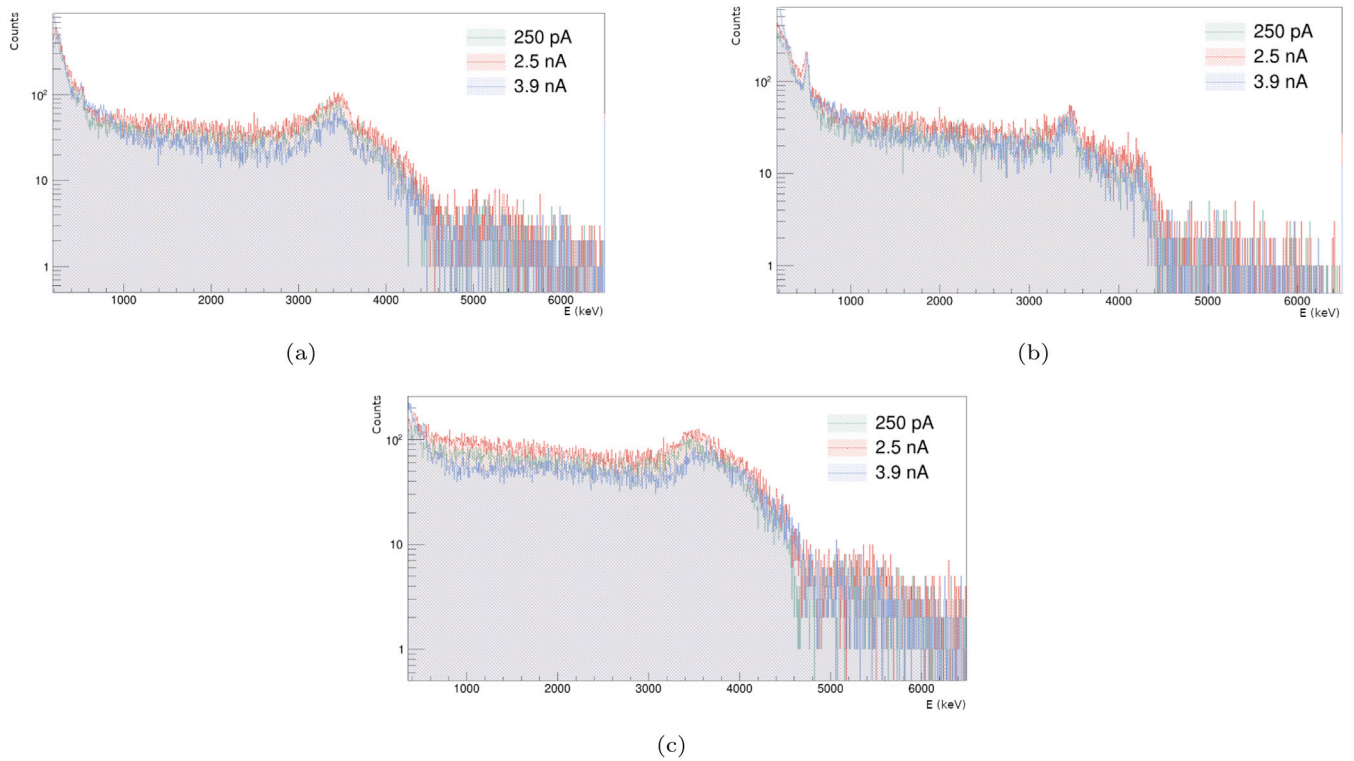
Fig. 5. Spectra measured in coincidence for the three currents by the first (a) and second (b) detector planes, as well as the summed energy spectra (c).
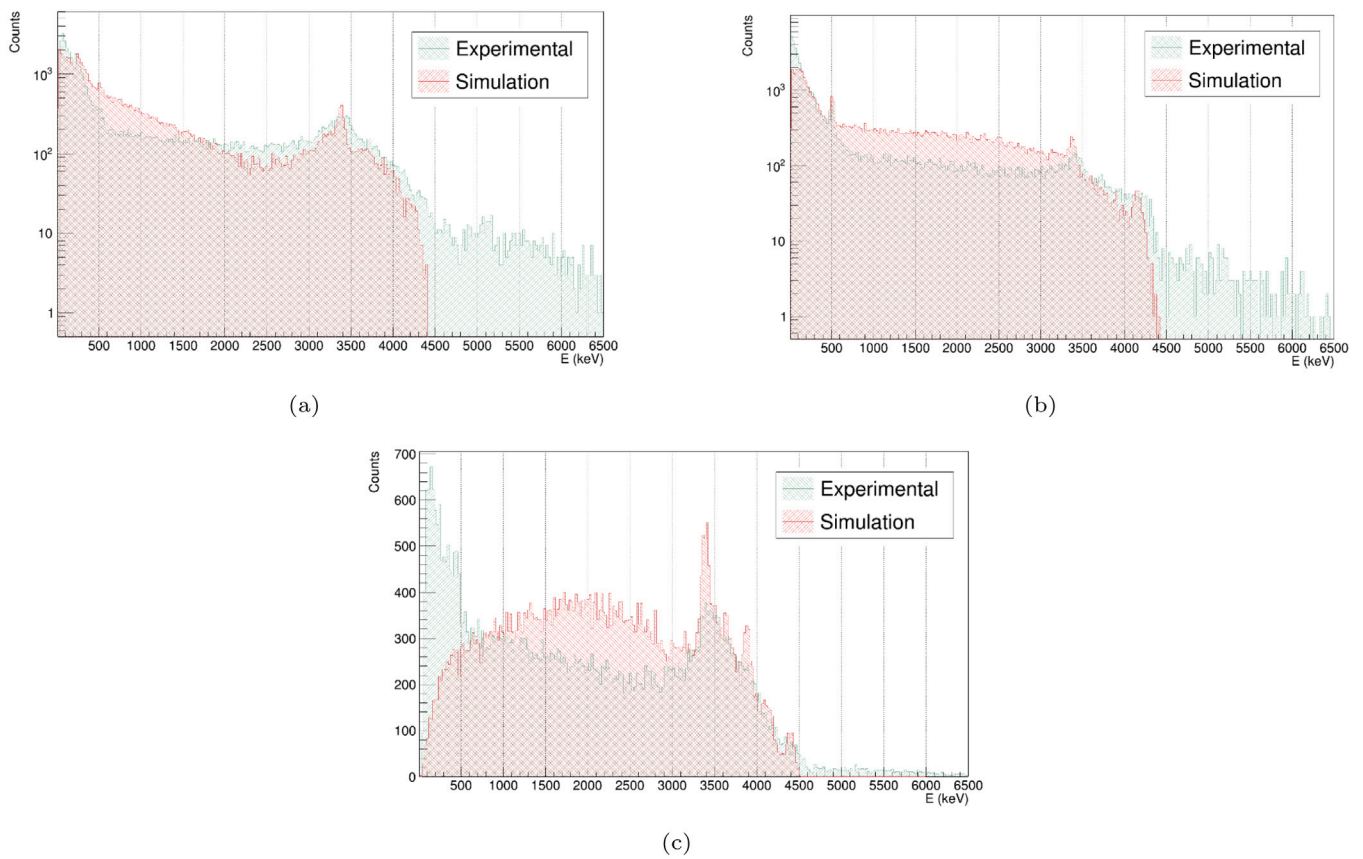

Fig. 6. Experimental and simulated energy spectra obtained in coincidence mode, with the low current beam, by the first (a) and second (b) detector planes, as well as the summed energy spectra (c).
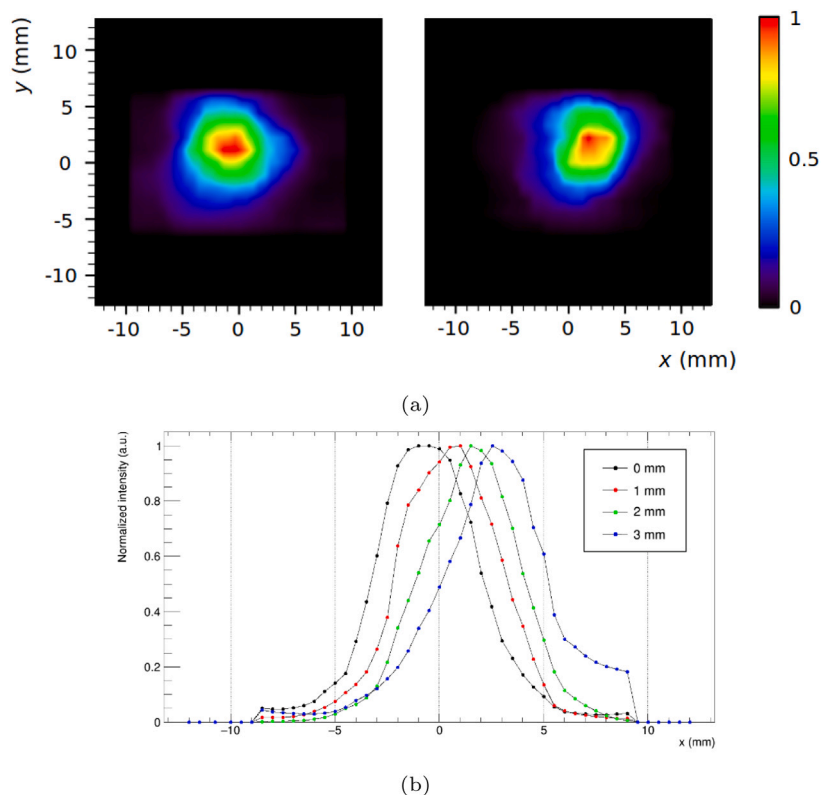
(a)

(b)

Fig. 7. (a) Reconstructed images of the fiftieth iteration of the photon emission distribution in two target positions 2 mm apart, measured with a nominal beam intensity of 250 pA and (b) *x*-profiles of the mentioned reconstruction. Acquisition time was 30 min.

Table 1
Calculated values for the absolute position and target separation for each reconstructed image.

Beam current (nA)	Target position	Absolute position (± 0.25 mm)			Target separation (± 0.35 mm)			
		Máx	R80	R50		Máx	R80	R50
0.25	0	−0.63	0.88	1.91	0 mm–1 mm	0.93	1.14	1.22
	1	0.59	1.81	3.05	1 mm–2 mm	1.01	0.85	1.16
	2	1.75	2.82	3.90	2 mm–3 mm	1.15	1.10	1.04
	3	2.79	3.97	5.00				
2.5	0	0.47	1.62	2.82	0 mm–2 mm	2.12	1.92	2.10
	2	2.59	3.54	4.92				
3.9	0	0.94	0.88	2.11	0 mm–2 mm	2.18	2.09	1.99
	2	3.12	2.27	4.20				

3.3.4. Detection efficiency

The intrinsic detection efficiency of MACACO$_p$ was calculated for the laboratory and in-beam measurements described in Sections 2.2 and 2.3.

The ε_{int} calculated with a ^{22}Na point-like source was of 7.7×10^{-3} and 8.5×10^{-3}, in the laboratory and through simulations, respectively.

For the in-beam measurements it was determined, through simulations, that 7.17×10^{-4} gammas are produced per emitted proton, when an 18 MeV proton beam is shot to a graphite target. The obtained yield was also cross-checked (taking into account the difference in beam energy and range) with the values stated by Pausch et al. (2020) and Fiedler et al. (2011), for pencil-beam scanning treatments with proton beam at the University Proton Therapy Dresden (Germany).

By using the mentioned production yield, an intrinsic detection efficiency of 6×10^{-3} was calculated from the experimental measurements at CNA. When the system is simulated, as detailed in Section 2.6, an efficiency of 3.32×10^{-3} is obtained.

4. Discussion and conclusion

MACACO$_p$, an alternative two-layer CC to the current MACACO II prototype of the IRIS group of IFIC-Valencia, was successfully developed and characterized. The obtained ER for both planes is comparable to the one obtained with MACACO II (5.6% and 6.6% FWHM at 511 keV) (Barrientos et al., 2021). After compensating for uncertainties in the recorded timestamps by means of time corrections, coincidence time resolutions of 820 ps FWHM and 1.50 ns FWHM were obtained with the detectors in PET and CC mode, respectively. These values show a great improvement when compared with the 24 ns obtained with MACACO II, and are to our knowledge among the best values reported in CC mode. Nevertheless, they still fall short when compared to the CTRs obtained in PET mode.

Several PET detector modules that employ the TOFPET2 ASIC (Table 2) are currently in development. The TOFPET2 ASIC was developed and optimized for the readout of detector modules composed of pixelated scintillator crystals coupled to SiPMs, and for an energy window around the 511 keV photopeak. Therefore, it is expected to obtain a

(a)

(b)

(c)

(d)
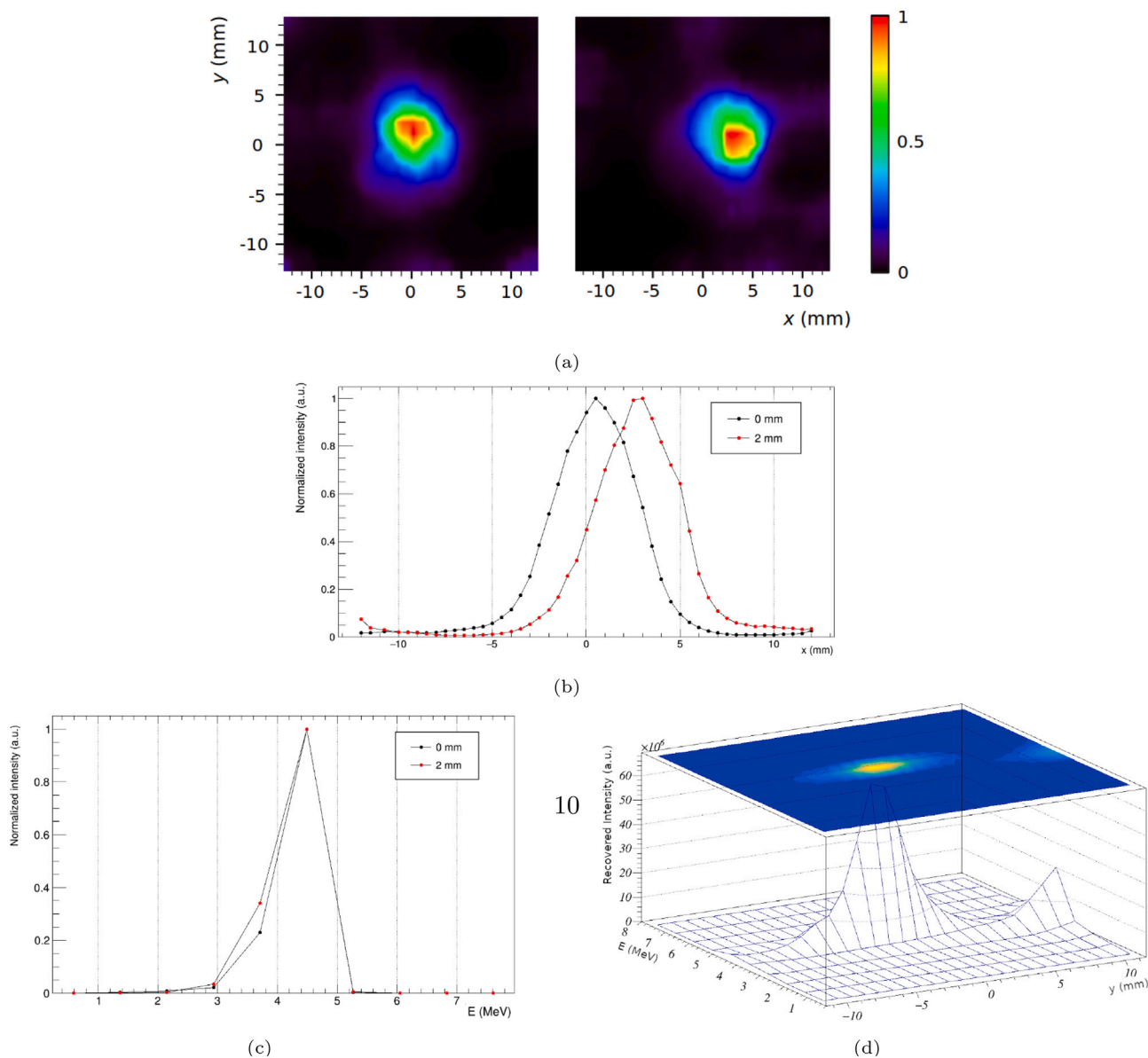
Fig. 8. (a) Reconstructed images of the fiftieth iteration of the photon emission distribution in two target positions 2 mm apart. (b) x-profiles and (c) E-profiles for the two different target positions measured with a nominal beam intensity of 2.5 nA. (d) yE-projection for the central target position. Acquisition time was 10 min.

better CTR when employing such type of crystals, as in Makek et al. (2020) and Yoshida et al. (2021). When using monolithic crystals, there is a wide spread of the scintillation light, resulting in a poor collection of optical photons and a low signal-to-noise ratio, and consequently a worse time resolution. Semi-monolithic crystals consist of a monolithic crystal segmented in one direction, combining the benefits of both pixelated and monolithic scintillator, having the best reported CTR (Cucarella et al., 2021) when employing the TOFPET2 ASIC. In addition, Table 3 lists some examples of detector modules in development for PET, that employ monolithic scintillation crystals, and a readout other than the TOFPET2 ASIC. CTRs between 200 ps and 500 ps have been reported (Borghi et al., 2018; Marcinkowski et al., 2016), when using digital SiPMs (dSiPM). In Sanchez et al. (2022) the 16-channel HRFlexToT was used as readout electronics. Several characteristics of the setup employed might have contributed to degrade the time resolution in the present work. Namely, the low acquisition thresholds can result in the detection of false triggers, introducing uncertainty in the timestamps. The crystal encapsulation further contributes to the spread of the optical photons. Moreover, the PCBs used as interface

between the SiPM array and the board that employs the ASIC may introduce additional noise.

Although the time resolution is an important characteristic of a CC, not many results in this regard have been reported. One cannot make a direct comparison with other CCs in development, due to the different materials, geometries and readout systems employed. Calderón (2014) and Jiang et al. (2021) reported CTRs, measured with a radioactive source placed between the modules (PET mode), of 12 ns and 7.5 ns FWHM, respectively. Golnik et al. (2016) published a CTR, measured in CC mode, of 4.9 ns FWHM. The time resolution of 1.50 ns FWHM (CC mode) obtained with $MACACO_p$ is therefore an improvement over the results reported so far in the literature in CC mode.

The $MACACO_p$ prototype was successfully tested with 4.44 MeV photons. The dynamic range of the ASIC allowed to obtain energy spectra up to 5 MeV, similar to the ones obtained with the PMT (Fig. 4). Fig. 6 shows the comparison between the measured and simulated spectra in coincidence mode, at high photon energies. Some mismatches between both scenarios are noticeable, specially at lower energies, mostly due to background in the experimental data. The simulation was
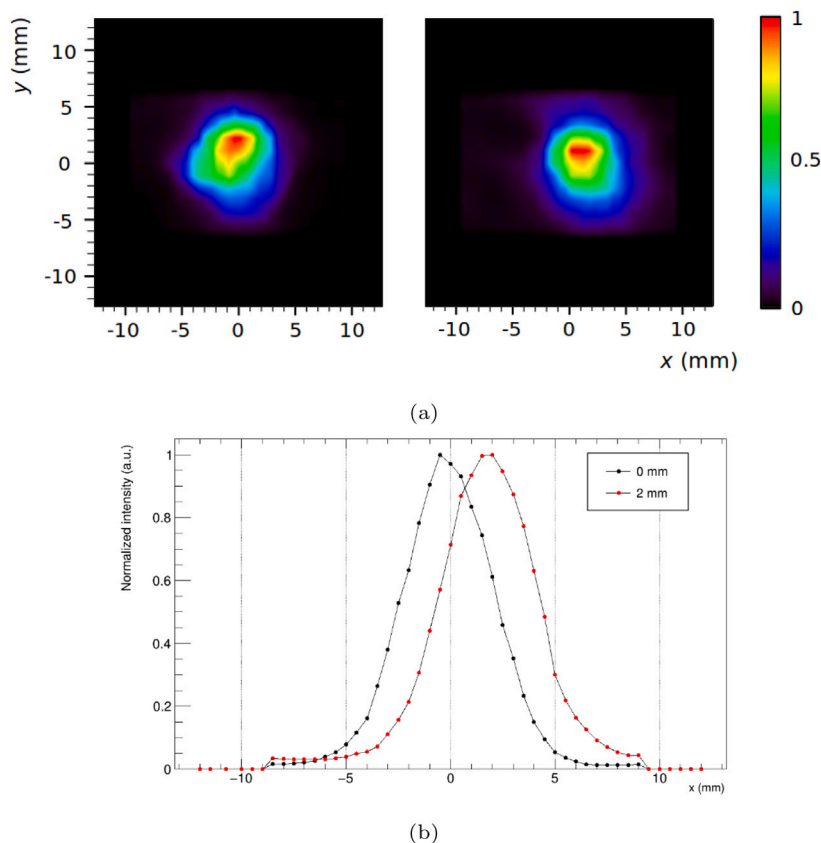
(a)

(b)

Fig. 9. (a) Reconstructed image of the fiftieth iteration of the photon emission distribution in two target positions 2 mm apart. (b) *x*-profiles of the two different target positions measured, with a nominal beam intensity of 3.9 nA. Acquisition time was 10 min.

Table 2
Coincidence time resolution, at FWHM, obtained with different detector modules in development, measuring in PET mode.

Reference	Crystal	SiPM (8 × 8 MPPC)	CTR (ps)	Temperature (°C)
Makek et al. (2020)	8 × 8 GaGG_Ce array	S13361-080AE, Hamamatsu	511	18.5 ± 0.5
Yoshida et al. (2021)	14 × 14 GFAG array	S14161-9865, Hamamatsu	531	23
Cucarella et al. (2021)	Semi-monolithic LYSO	S13361-3050AE-08, Hamamatsu	280	19 ± 1
Lamprou et al. (2020)	Monolithic LYSO	ON-seni, J-series model	660	7

Table 3
Coincidence time resolution obtained with different PET detector modules, that employ monolithic scintillation crystals and a readout different than the TOFPET2 ASIC.

Reference	Crystal (monolithic)	SiPM	CTR (ps)
Borghi et al. (2018)	LYSO	DPC3200-22-44 (dSiPM), Philips	212
Sanchez et al. (2022)	LFS	S13361-6050NE-04, Hamamatsu	324
Marcinkowski et al. (2016)	LYSO	DPC3200-22-44 (dSiPM), Philips	529

performed with a 4.44 MeV gamma source (Section 2.6), therefore it does not take into account the irradiation of the graphite target with protons. In the experimental scenario, the target will act as a 511 keV emitter, after being irradiated, and therefore more coincidences at low energies can be observed in this case.

Figs. 8(b) and 8(c) depict the energy profile and yE-projection, respectively, for the centre target position, for a beam current 2.5 nA, as an overall example. The target was placed at different positions to study the system's capability of detecting range shifts. The maximum, R80 and R50 of the reconstructed longitudinal profiles were evaluated for each target position and are presented in Table 1. The measured target separation, for all current beams, is within the expected value. The obtained results show the ability of the system to detect 1 mm variations in the photon emission distribution for low current beams and 2 mm for higher current beams. The employed spectral image reconstruction code, which makes no assumption on the incident photon energy, was successfully used to recover the spot at the expected 4.44 MeV PG energy, even though this photopeak is hardly visible in the obtained spectra.

The MACACO II feasibility for reconstructing images of the photon emission distribution at 4.44 MeV at the CNA was reported in a previous work (Ros et al., 2020), in which images were successfully reconstructed at target positions separated by 5 mm. The results obtained with MACACO$_p$ presented in this work show a significantly improved performance with respect to MACACO II.

An experimental estimation of the intrinsic detection efficiency both at low and high energies was also carried out, which can be employed in future studies of its viability for real-time monitoring. An experimental detection efficiency of 7.7×10^{-3} at the laboratory and of 6×10^{-3} at high photon energies, were obtained with an interplane distance of 60 mm. The experimental results are in agreement with the simulated ones. The reported values are comparable with the 1×10^{-3}

obtained with MACACO II, for the same interplane distance (Barrientos et al., 2021). The system's efficiency can be further increased by using larger detector modules, however this will not translate into a linear increase. Moreover there are other considerations to have in mind when increasing the detector sizes. For example, the number of readout channels would need to be incremented, which would not only make the system more complex but also significantly increase the data processing time. A more detailed study regarding the increase of the efficiency is currently undergoing, through simulations.

The results obtained with MACACO$_p$ show it is a promising system for hadron therapy monitoring. Its improved time resolution and higher dynamic range make it a suited alternative to MACACO II. To further improve the CC prototype, namely its time and energy resolution, a new setup is in development, where the adapter PCB will be replaced by flat cables and an efficient temperature controlling system will be employed. Moreover, a third plane will be added to the CC, with the purpose of combining both two- and three-layer acquisition modalities, to maximize the system's resolution and efficiency. Studies are undergoing to improve the reconstructed image quality, through the removal of background events via hardware (Borja-Lloret et al., 2022) and software (Muñoz et al., 2021; Roser et al., 2022). In addition, different photodetectors are being tested as well as bigger scintillator crystals, to increase the detector's size. Likewise, MACACO III, an improved version of MACACO II, was developed and is being characterized.

CRediT authorship contribution statement

R. Viegas: Methodology, Software, Investigation, Writing – review & editing, Visualization. **J. Roser:** Methodology, Software, Writing – review & editing. **L. Barrientos:** Writing – review & editing. **M. Borja-Lloret:** Software, Writing – review & editing. **J.V. Casaña:** Writing – review & editing. **J. García López:** Resources. **M.C. Jiménez-Ramos:** Resources. **F. Hueso-González:** Software, Writing – review & editing. **A. Ros:** Validation, Supervision. **G. Llosá:** Conceptualization, Validation, Writing – review & editing, Supervision, Project administration, Funding acquisition.

Declaration of competing interest

The authors declare that they have no known competing financial interests or personal relationships that could have appeared to influence the work reported in this paper.

Data availability

Data will be made available on request.

Acknowledgements

References

Agostinelli, S., et al., 2003. Geant4—A simulation toolkit. Nucl. Instrum. Methods Phys. Res. A 506 (3), 250–303. http://dx.doi.org/10.1016/S0168-9002(03)01368-8.

Ahmad, S., Blin, S., Callier, S., Cizel, J., Conforti, S., de La Taille, C., Dulucq, F., Fleury, J., Martin-Chassard, G., Raux, L., 2021. OMEGA SiPM readout ASICs. Nucl. Instrum. Methods Phys. Res. A 986, 164628. http://dx.doi.org/10.1016/j.nima.2020.164628.

Ahmad, S., Fleury, J., de la Taille, C., Seguin-Moreau, N., 2020. Recent developments in fast timing ASICs for particle physics and medical imaging. Il Nuovo Cimento 43 (1), http://dx.doi.org/10.1393/ncc/i2020-20004-9.

Baratto-Roldán, A., Jiménez-Ramos, M., Battaglia, M., García-López, J., Gallardo, M., Cortés-Giraldo, M., Espino, J., 2018. Feasibility study of a proton irradiation facility for radiobiological measurements at an 18 MeV cyclotron. Instruments 2 (4), 26. http://dx.doi.org/10.3390/instruments2040026.

Barrientos, L., Borja-Lloret, M., Etxebeste, A., Muñoz, E., Oliver, J., Ros, A., Roser, J., Senra, C., Viegas, R., Llosá, G., 2021. Performance evaluation of Macaco III Compton camera. Nucl. Instrum. Methods Phys. Res. A 1014, 165702. http://dx.doi.org/10.1016/j.nima.2021.165702.

Barrio, J., Etxebeste, A., Lacasta, C., Muñoz, E., Oliver, J., Solaz, C., Llosá, G., 2015. Performance of VATA64HDR16 ASIC for medical physics applications based on continuous crystals and SiPMs. J. Instrum. 10 (12), P12001. http://dx.doi.org/10.1088/1748-0221/10/12/P12001.

Biegun, A., Lopes, P.C., Rinaldi, I., Oxley, D., Seravalli, E., Verhaegen, F., Dendooven, P., Parodi, K., Schaart, D., Crespo, P., et al., 2012. Time-of-flight method for neutron rejection in prompt gamma imaging of beam range and density changes in proton therapy. Radiother. Oncol. 102, http://dx.doi.org/10.1016/s0167-8140(12)70226-8.

Borghi, G., Tabacchini, V., Bakker, R., Schaart, D.R., 2018. Sub-3 mm, near-200 ps TOF/doi-pet imaging with monolithic scintillator detectors in a 70 cm diameter tomographic setup. Phys. Med. Biol. 63 (15), 155006. http://dx.doi.org/10.1088/1361-6560/aad2a6.

Borja-Lloret, M., Barrientos, L., Bernabéu, J., Lacasta, C., Muñoz, E., Ros, A., Roser, J., Viegas, R., Llosá, G., 2022. Study of the background in hadron therapy treatment monitoring with a Compton camera. in preparation.

Bugalho, R., Di Francesco, A., Ferramacho, L., Leong, C., Niknejad, T., Oliveira, L., Pacher, L., Rolo, M., Rivetti, A., Silveira, M., 2018. Experimental results with TOFPET2 ASIC for time-of-flight applications. Nucl. Instrum. Methods Phys. Res. A 912, 195–198. http://dx.doi.org/10.1016/j.nima.2017.11.034.

Bugalho, R., Francesco, A.D., Ferramacho, L., Leong, C., Niknejad, T., Oliveira, L., Rolo, M., Silva, J., Silva, R., Silveira, M., 2019. Experimental characterization of the TOFPET2 ASIC. J. Instrum. 14 (03), http://dx.doi.org/10.1088/1748-0221/14/03/p03029.

Calderón, Y., 2014. Design, Development, and Modeling of a Compton camera Tomographer Based on Room Temperature Solid State Pixel Detector (Ph.D. thesis).

Cucarella, N., Barrio, J., Lamprou, E., Valladares, C., Benlloch, J.M., González, A.J., 2021. Timing evaluation of a pet detector block based on semi-monolithic LYSO crystals. Med. Phys. 48 (12), 8010–8023. http://dx.doi.org/10.1002/mp.15318.

van Dam, H.T., Borghi, G., Seifert, S., Schaart, D.R., 2013. Sub-200 ps CRT in monolithic scintillator PET detectors using digital SiPM arrays and maximum likelihood interaction time estimation. Phys. Med. Biol. 58 (10), 3243–3257. http://dx.doi.org/10.1088/0031-9155/58/10/3243.

Ferramacho, L., Tavernier, S., 2019. Untitled manuscript. private communication.

Fiedler, F., Dersch, U., Golnik, C., Kormoll, T., Muller, A., Rohling, H., Schone, S., Enghardt, W., 2011. The use of prompt gamma-rays for in-vivo dosimetry at therapeutic proton and ion beams. In: 2011 IEEE Nuclear Science Symposium Conference Record. http://dx.doi.org/10.1109/nssmic.2011.6152493.

Francesco, A.D., Bugalho, R., Oliveira, L., Pacher, L., Rivetti, A., Rolo, M., Silva, J., Silva, R., Varela, J., 2016. TOFPET2: A high-performance ASIC for time and amplitude measurements of SiPM signals in time-of-flight applications. J. Instrum. 11 (03), http://dx.doi.org/10.1088/1748-0221/11/03/c03042.

Golnik, C., Bemmerer, D., Enghardt, W., Fiedler, F., Hueso-González, F., Pausch, G., Römer, K., Rohling, H., Schöne, S., Wagner, L., 2016. Tests of a compton imaging prototype in a monoenergetic 4.44 MeV photon field—A benchmark setup for prompt gamma-ray imaging devices. J. Instrum. 11 (06), http://dx.doi.org/10.1088/1748-0221/11/06/p06009.

Hueso-González, F., Bortfeld, T., 2020. Compact method for proton range verification based on coaxial prompt gamma-ray monitoring: A theoretical study. IEEE Trans. Radiat. Plasma Med. Sci. 4 (2), 170–183. http://dx.doi.org/10.1109/trpms.2019.2930362.

Hueso-Gonzalez, F., Pausch, G., Petzoldt, J., Romer, K.E., Enghardt, W., 2017. Prompt gamma rays detected with a BGO block Compton camera reveal range deviations of therapeutic proton beams. IEEE Trans. Radiat. Plasma Med. Sci. 1 (1), 76–86. http://dx.doi.org/10.1109/tns.2016.2622162.

Jan, S., Benoit, D., Becheva, E., Carlier, T., Cassol, F., Descourt, P., Frisson, T., Grevillot, L., Guigues, L., Maigne, L., et al., 2011. GATE V6: A major enhancement of the GATE simulation platform enabling modelling of CT and radiotherapy. Phys. Med. Biol. 56 (4), 881. http://dx.doi.org/10.1088/0031-9155/56/4/001.

Jiang, S., Lu, J., Meng, S., Ye, F., Ning, J., Yi, Q., Yang, J., Yang, R., Yan, X., 2021. A prototype of SIPM-based scintillator Compton camera with capacitive multiplexing readout. J. Instrum. 16 (01), http://dx.doi.org/10.1088/1748-0221/16/01/p01027.

Krimmer, J., Dauvergne, D., Létang, J., Testa, É., 2018. Prompt-gamma monitoring in hadrontherapy: A review. Nucl. Instrum. Methods Phys. Res. A 878, 58–73. http://dx.doi.org/10.1016/j.nima.2017.07.063.

Lamprou, E., González, A.J., Sanchez, F., Benlloch, J.M., 2020. Exploring TOF capabilities of PET detector blocks based on large monolithic crystals and analog SiPMs. Phys. Medica 70, 10–18. http://dx.doi.org/10.1016/j.ejmp.2019.12.004.

Liprandi, S., Mayerhofer, M., Aldawood, S., Binder, T., Dedes, G., Miani, A., Schaart, D.R., Lozano, I.I., Parodi, K., Thirolf, P.G., 2017. Sub-3mm spatial resolution from a large monolithic labr3 (CE) scintillator. Curr. Directions Biomed. Eng. 3 (2), 655–659. http://dx.doi.org/10.1515/cdbme-2017-0138.

Livingstone, J., Dauvergne, D., Etxebeste, A., Fontana, M., Gallin-Martel, M.-L., Huisman, B., Létang, J.M., Marcatili, S., Sarrut, D., Testa, É., 2021. Influence of sub-nanosecond time of flight resolution for online range verification in proton therapy using the line-cone reconstruction in Compton imaging. Phys. Med. Biol. 66 (12), 125012. http://dx.doi.org/10.1088/1361-6560/ac03cb.

Llosá, G., 2019. SiPM-based Compton cameras. Nucl. Instrum. Methods Phys. Res. A 926, 148–152. http://dx.doi.org/10.1016/j.nima.2018.09.053.

Makek, M., Bosnar, D., Koauljević, A.M., Pavelić, L., 2020. Investigation of GAGG:CE with Tofpet2 ASIC readout for applications in Gamma imaging systems. Crystals 10 (12), 1073. http://dx.doi.org/10.3390/cryst10121073.

Marcinkowski, R., Mollet, P., Van Holen, R., Vandenberghe, S., 2016. Sub-millimetre DOI detector based on monolithic LYSO and digital SIPM for a dedicated small-animal pet system. Phys. Med. Biol. 61 (5), 2196–2212. http://dx.doi.org/10.1088/0031-9155/61/5/2196.

Meier, D., Mikkelsen, S., Talebi, J., Azman, S., Mahlum, G., Patt, B.E., 2010. An ASIC for SIPM/MPPC readout. In: IEEE Nuclear Science Symposium Conference Record. http://dx.doi.org/10.1109/nssmic.2010.5874056.

Meißner, H., Fuchs, H., Hirtl, A., Reschl, C., Stock, M., 2019. Towards offline PET monitoring of proton therapy at MedAustron. Zeitschrift Für Medizinische Physik 29 (1), 59–65. http://dx.doi.org/10.1016/j.zemedi.2018.05.003.

Muñoz, E., Barrientos, L., Bernabéu, J., Borja-Lloret, M., Llosá, G., Ros, A., Roser, J., Oliver, J.F., 2020. A spectral reconstruction algorithm for two-plane Compton cameras. Phys. Med. Biol. 65 (2), 025011. http://dx.doi.org/10.1088/1361-6560/ab58ad.

Muñoz, E., Ros, A., Borja-Lloret, M., Barrio, J., Dendooven, P., Oliver, J.F., Ozoemelam, I., Roser, J., Llosá, G., 2021. Author correction: Proton range verification with Macaco II Compton camera enhanced by a neural network for event selection. Sci. Rep. 11 (1), http://dx.doi.org/10.1038/s41598-021-03252-5.

O'Neill, T., Ait-Ouamer, F., Schwartz, I., Tumer, O., White, R., Zych, A., 1992. Compton recoil electron tracking with silicon strip detectors. IEEE Trans. Nucl. Sci. 39 (4), 629–634. http://dx.doi.org/10.1109/23.159677.

Ortega, P.G., Torres-Espallardo, I., Cerutti, F., Ferrari, A., Gillam, J.E., Lacasta, C., Llosá, G., Oliver, J.F., Sala, P.R., Solevi, P., 2015. Noise evaluation of Compton camera imaging for proton therapy. Phys. Med. Biol. 60 (5), 1845–1863. http://dx.doi.org/10.1088/0031-9155/60/5/1845.

Paganetti, H., 2012. Range uncertainties in proton therapy and the role of Monte Carlo simulations. Phys. Med. Biol. 57 (11), http://dx.doi.org/10.1088/0031-9155/57/11/r99.

Parajuli, R.K., Sakai, M., Kada, W., Torikai, K., Kikuchi, M., Arakawa, K., Torikoshi, M., Nakano, T., 2019. Annihilation gamma imaging for carbon ion beam range monitoring using SI/CdTe Compton camera. Phys. Med. Biol. 64 (5), 055003. http://dx.doi.org/10.1088/1361-6560/ab00b2.

Pausch, G., Berthold, J., Enghardt, W., Römer, K., Straessner, A., Wagner, A., Werner, T., Kögler, T., 2020. Detection systems for range monitoring in proton therapy: Needs and challenges. Nucl. Instrum. Methods Phys. Res. A 954, 161227. http://dx.doi.org/10.1016/j.nima.2018.09.062.

Polf, J.C., Maggi, P., Panthi, R., Peterson, S., Mackin, D., Beddar, S., 2022. The effects of Compton camera data acquisition and readout timing on PG imaging for proton range verification. IEEE Trans. Radiat. Plasma Med. Sci. 6 (3), 366–373. http://dx.doi.org/10.1109/trpms.2021.3057341.

Poulson, D., Bloser, P., Ogasawara, K., Trevino, J., Legere, J., Ryan, J., McConnell, M., 2020. Development of a compton telescope based on single-crystal diamond detectors and fast scintillators. In: Space Telescopes and Instrumentation 2020: Ultraviolet to Gamma Ray. http://dx.doi.org/10.1117/12.2576091.

Ros, A., Barrientos, L., Borja-Lloret, M., Casaña, J., Muñoz, E., Roser, J., Udías, J., Viegas, R., Llosá, G., 2021. New probe for the improvement of the spatial resolution in total-body pet (PROScRiPT). EPJ Web Conf. 253, 09004. http://dx.doi.org/10.1051/epjconf/202125309004.

Ros, A., Barrio, J., Etxebeste, A., García López, J., Jiménez-Ramos, M.C., Lacasta, C., Muñoz, E., Oliver, J.F., Roser, J., Llosá, G., 2020. MACACO II test-beam with high energy photons. Phys. Med. Biol. 65 (24), 245027. http://dx.doi.org/10.1088/1361-6560/abc5cd.

Roser, J., Barrientos, L., Bernabéu Alberola, J., Borja-Lloret, M., Muñoz, E., Ros, A., Viegas, R., Llosá, G., 2022. Joint image reconstruction algorithm in Compton cameras. Phys. Med. Biol. http://dx.doi.org/10.1088/1361-6560/ac7b08.

Sanchez, D., Gomez, S., Mauricio, J., Freixas, L., Sanuy, A., Guixe, G., Lopez, A., Manera, R., Marin, J., Perez, J.M., 2022. HRFlexToT: A high dynamic range ASIC for time-of-flight positron emission tomography. IEEE Trans. Radiat. Plasma Med. Sci. 6 (1), 51–67. http://dx.doi.org/10.1109/trpms.2021.3066426.

Todd, R.W., Nightingale, J.M., Everett, D.B., 1974. A proposed γ camera. Nature 251 (5471), 132–134. http://dx.doi.org/10.1038/251132a0.

Verburg, J.M., Riley, K., Bortfeld, T., Seco, J., 2013. Energy- and time-resolved detection of prompt gamma-rays for proton range verification. Phys. Med. Biol. 58 (20), http://dx.doi.org/10.1088/0031-9155/58/20/l37.

Verburg, J.M., Seco, J., 2014. Proton range verification through prompt gamma-ray spectroscopy. Phys. Med. Biol. 59 (23), 7089–7106. http://dx.doi.org/10.1088/0031-9155/59/23/7089.

Yamaya, T., Yoshida, E., Inaniwa, T., Sato, S., Nakajima, Y., Wakizaka, H., Kokuryo, D., Tsuji, A., Mitsuhashi, T., Kawai, H., 2011. Development of a small prototype for a proof-of-concept of openpet imaging. Phys. Med. Biol. 56 (4), 1123–1137. http://dx.doi.org/10.1088/0031-9155/56/4/015.

Yoshida, E., Akamatsu, G., Tashima, H., Kamada, K., Yoshikawa, A., Yamaya, T., 2021. First imaging demonstration of a crosshair light-sharing pet detector. Phys. Med. Biol. 66 (6), 065013. http://dx.doi.org/10.1088/1361-6560/abe839.